

Self-consistent simulation of the photoelectron-driven polar wind from 120 km to 9 R_E altitude

Yi-Jiun Su, J. L. Horwitz, G. R. Wilson,¹ P. G. Richards, and D. G. Brown

Center for Space Plasma, and Aeronomic Research, The University of Alabama in Huntsville
Huntsville, Alabama

C. W. Ho

Department of Physics, Prairie View A&M University, Prairie View, Texas

Abstract. It has long been recognized that photoelectrons can enhance the ambipolar electric fields affecting polar wind outflows [e.g., *Axford*, 1968; *Lemaire*, 1972]. Since ionospheric ions and electrons are produced in large part by photoionization of the neutral atmosphere at lower altitudes, and the maximum photoelectron production rate occurs in the 130–140 km altitude range, it is essential to model this photoelectron-driven polar wind self-consistently from the E region to an altitude of several Earth radii. Here we describe a new steady state coupled fluid-semikinetetic model to efficiently couple the source region to the high-altitude regions. This model couples a fluid treatment for the 120–800 km altitude range, a generalized semikinetetic (GSK) treatment for the altitude range 800 km to 2 R_E , and a steady state collisionless semikinetetic method for the altitude range 2–9 R_E . We apply this model to investigate the photoelectron-driven polar wind with ionospheric conditions ranging from solar minimum ($F_{10.7} = 90$) to solar maximum ($F_{10.7} = 200$). The O^+ and H^+ densities are found to increase by factors of approximately 5 and 2, respectively, from solar minimum to solar maximum below 3 R_E altitude. However, the parallel bulk velocities display little variation with increased $F_{10.7}$ for altitudes below 3 R_E . An electric potential layer of the order of 40 V develops above 3 R_E altitude, when the included downward magnetosheath electron fluxes (such as polar rain) are insufficient to balance the ionospheric photoelectron flux. Such potential layers accelerate the ionospheric ions to supersonic speeds at high altitudes, above 3 R_E , but not at low altitudes. We also found that the potential layer decreases from 40 to 8.5 V for solar minimum conditions and from 46 to 12 V for solar maximum conditions when the magnetospheric electron density is increased from 0.05 to 2 cm^{-3} .

1. Introduction

In the 1960s it was suggested that light ionospheric ions (H^+ and He^+) might be able to escape along “open” magnetic field lines from the topside ionosphere into the tail regions of the magnetosphere via an evaporative process [e.g., *Bauer*, 1966; *Dessler and Michel*, 1966]. *Axford* [1968] argued that the outflow of plasma should be supersonic and referred to it as the “polar wind” in analogy to the solar wind. A simple hydrodynamic description predicted supersonic ion outflow at

2000–5000 km altitudes [e.g., *Banks and Holzer*, 1968, 1969], while *Lemaire and Scherer* [1970] obtained similar results using a semikinetetic evaporation-based theory.

Direct observations of the polar wind were first made on Explorer 31 (at an altitude range of 500 to 3000 km) and ISIS 2 (in a circular polar orbit at 1400 km) satellites [*Hoffman*, 1970; *Hoffman et al.*, 1974; *Hoffman and Dodson*, 1980]. The results confirmed that an upward flow of both H^+ and He^+ ions exists at all times over the entire polar region. Supersonic H^+ flows along high-latitude field lines were observed for the first time by the retarding ion mass spectrometer (RIMS) on Dynamics Explorer (DE) 1 [*Nagai et al.*, 1984; *Olsen et al.*, 1986], in general accord with classical polar wind model results.

The expansion of ionospheric plasma along polar field lines may be characterized by three regions. The first region extends from approximately 80 km altitude up

¹Now at Mission Research Corporation, Nashua, New Hampshire.

to 800 km where ion-ion and ion-neutral collisions are dominant. Molecular ions (N_2^+ , O_2^+ , NO^+) dominate below the F_1 peak (about 180 km altitude) where the ion dynamics are dominated by collisions with neutrals. Ionospheric ions and electrons are produced by photoionization of the neutral constituents. O^+ ions display a significant upward or downward characteristic drift at high latitudes [Loranc *et al.*, 1991], which varies considerably depending on the flux tube's history of convection, electron precipitation, and other characteristics. An ambipolar electric field produced between the heavy O^+ ions and light electrons acts to decelerate and accelerate the flow of electrons and ions, respectively, so as to maintain quasi-neutrality and low or zero current. Hydrogen ions are created due to the accidentally resonant charge exchange reaction $O^+ + H \rightarrow O + H^+$ and are subsequently accelerated upward along the geomagnetic field by the ambipolar electric field. Since O^+ charge exchange is the main source for H^+ and also determines the magnitude of the ambipolar electric field, a self-consistent model of the polar wind must include both the O^+ and H^+ source regions. In this region, ion-ion self-collisions prevail, and if convection is slow, the temperature distribution is isotropic, and the heat flow is proportional to the temperature gradient.

The second region may be referred to as the transition region, in which the dominant ion changes from O^+ to H^+ and the plasma becomes nearly collisionless. H^+ and O^+ production/loss processes are unimportant in this region. Depending on the precise definition, the transition region will vary in range but can be said to be approximately 1000 to 5000 km. The competing effects of the ambipolar electric field acceleration of H^+ and collisional drag with O^+ lead to non-Maxwellian H^+ velocity distributions, including downwardly stretched tails or heat fluxes [e.g., Wilson, 1992]. This region is complicated because H^+-O^+ collisions tend to distort the H^+ velocity distribution, while H^+ self-collisions tend to thermalize them, but this thermalization is not complete because of the long self-collision relaxation times compared to the ion transport times [Wilson, 1995; Ho *et al.*, 1997].

The third region spans the top of the transition region at about 5000 km to several R_E and is characterized by collisionless flow, defined as the collisional mean free path being much greater than the magnetic and plasma scale heights. In the collisionless regime, ion distribution functions may be highly non-Maxwellian, including the presence of strong parallel heat fluxes, conics, rings, and multiple streams, which often occur because of auroral processes. The mathematical formulation of such polar plasma transport, including the description of energized heavy ions and allowing for large heat flows and temperature anisotropies, is considerably more complicated.

The collision-dominated characteristics of the flow have been extensively studied with hydrodynamic (fluid)

steady state models [Banks and Holzer, 1968, 1969; Marubashi, 1970; Raitt *et al.*, 1975, 1977, 1978a, b; Schunk and Nagy, 1978; Barakat and Schunk, 1984b; Barakat *et al.*, 1987; Moore, 1980; Ottley and Schunk, 1980]. In the higher-altitude, nearly collisionless regime the mathematical formulation of the polar plasma transport is considerably more complicated. This collisionless regime has been modeled with hydromagnetic [Holzer *et al.*, 1971], kinetic [Lemaire, 1972; Lemaire and Scherer, 1973], and semikinetical [Barakat and Schunk, 1983, 1984a; Li *et al.*, 1988] treatments. Also, generalized transport equations that include both collision-dominated and collisionless characteristics of ion outflow have been used. Schunk and Watkins [1981, 1982] have studied a fully ionized H^+-O^+ -electron anisotropic plasma along geomagnetic field lines from 1500 km up to 12,000 km altitude based on the 13-moment system of transport equations. Demars and Schunk [1986, 1987] have used the bi-Maxwellian-based 16-moment transport equations for applications to the polar wind and related problems. These aforementioned studies of the classical polar wind were for steady state conditions with emphasis on elucidating the physical process. In the past 10 years, attention has been focused on studying the temporal characteristics of the polar wind. Hence time-dependent hydrodynamic models [Singh and Schunk, 1985; Gombosi *et al.*, 1985; Gombosi and Killeen, 1987; Gombosi and Schunk, 1988; Schunk and Sojka, 1989; Ganguli, 1986; Ganguli and Palmadesso, 1987; Ganguli *et al.*, 1987] and time-dependent generalized semikinetical (GSK) models [e.g., Wilson *et al.*, 1990; Wilson, 1992; Brown *et al.*, 1995; Ho *et al.*, 1997] have been developed.

It has been recognized that the presence of suprathermal electrons, such as photoelectrons produced in the upper atmosphere during the ionization of neutral species by solar EUV radiation, can enhance the ambipolar electric fields that propel polar wind outflows [e.g., Axford, 1968; Lemaire, 1972]. Axford [1968] suggested that a flux of $2 \times 10^8 \text{ cm}^{-2} \text{ s}^{-1}$ of escaping photoelectrons is required to draw out of the polar ionosphere all the He^+ ions produced in the atmosphere. Collisionless kinetic calculations by Lemaire [1972] have shown that the additional electric force due to the escaping photoelectrons can accelerate the ions to higher velocities if the photoelectron flux is larger than the escape flux of the thermal electrons in the polar wind.

Winningham and Gurgiolo [1982] and Horwitz *et al.* [1992] have reported indications of significant potentials of the order of 5–40 V, distributed along polar magnetic field lines, and have suggested a possible association with atmospheric photoelectrons. The effects of hot magnetospheric electrons, such as polar rain, have been investigated, though with rather incomplete methods, by Barakat and Schunk [1984a] and Ho *et al.* [1992]. Suprathermal electrons also transfer energy to other plasma components through collisions and waves

[e.g., Khazanov *et al.*, 1994]. Akebono observations have shown that the polar wind velocity was generally higher on the dayside than on the nightside and was strongly correlated with the ambient electron temperature [Abe *et al.*, 1993a, b]. The correlation was strongest, that is, the relative increase in ion velocity with electron temperature was largest, at high altitude. This result may be attributable to the cumulative effect of ion acceleration due to the ambipolar electric field along the field line. Yau *et al.* [1995] have reported Akebono observations of anisotropic electron velocity distributions in the sunlit polar wind, in which the average energy (temperature) of the thermal electrons is higher in the upward magnetic field direction than in the downward and perpendicular directions. Yasseen *et al.* [1989] showed that the ionospheric photoelectrons are the source of both the upward suprathermal field-aligned electron fluxes obtained at high altitudes (22,400 km), and the downward fluxes, obtained at low altitudes (600 km; see their Figure 1), reflected by an assumed upward electric field.

Tam *et al.* [1995] showed that the suprathermal photoelectron contribution to the heat flux dominated that of the thermal electrons obtained from a self-consistent generalized fluid calculation, and they argued, using quasi-neutrality and current-free constraints, that photoelectrons may significantly increase the ambipolar electric fields, which, in turn, should increase ion flow velocities. They suggested that the photoelectron-enhanced electric field may play a significant role in propelling the polar wind in the dayside polar region. A more recent collisionless semikinetic model for achieving zero current for polar wind outflow on open flux tubes by Wilson *et al.* [1997] has indicated a 45–60 V discontinuous potential drop which may reflect most of the photoelectrons back toward the ionosphere.

However, these models [Tam *et al.*, 1995; Wilson *et al.*, 1997] adopted 500 km altitude boundary conditions, and since ionospheric ions and electrons are produced in large part by photoionization of the neutral atmosphere at lower altitudes, the models are incomplete and not self-consistent. These photoionization processes occur primarily below 500 km altitude, and the maximum photoelectron production rate occurs in the 130–140 km altitude range.

Therefore a truly self-consistent model of the photoelectron-driven polar wind should ideally incorporate and properly couple to the lower-altitude sources of both the ionosphere thermal plasmas and the suprathermal photoelectrons. We have therefore developed a coupled fluid-semikinetic model for ionospheric plasma outflow with photoelectron inclusion of effects on the parallel driving electric field. This model uses a procedure for describing the ionosphere with a low-speed fluid treatment for the 120–800 km altitude range, coupling this fluid treatment to a GSK treatment [Wilson, 1992, 1994] for the altitude range 800 km to $2 R_E$ and

then coupling this treatment to a steady state collisionless semikinetic treatment with Liouville mapping for altitudes from 2 to $9 R_E$. In this paper we apply this model, including photoelectron production and ionization using a two-stream treatment for photoelectrons at lower altitudes, to investigate photoelectron effects on the polar wind from the ionospheric plasma and photoelectron source region to the high-altitude regions for different solar and ionospheric conditions, as well as magnetosheath particle conditions at the upper portion of the flux tube.

2. Model Description

Mean free path estimates indicate that the polar wind is collision-dominated (mean free path \ll plasma scale height) at low altitudes (≤ 1000 – 2000 km) and collisionless at higher altitudes (≥ 3000 km). Although several models have been developed for studying the polar wind, neither purely fluid-based nor purely semikinetic methods are likely to be adequate for accurately and efficiently modeling the ionospheric plasma outflow from the *F* region (the source of the polar wind) to high altitudes. It is inaccurate to use a fluid treatment for describing the non-Maxwellian ion distribution functions in the higher-altitude, nearly collisionless regimes, and it is computationally infeasible or at least inefficient to use a semikinetic treatment for the ions in the lower ionosphere, where the high densities involve very large numbers of simulation ions and timescales for collisional and chemistry processes are short. Therefore coupling a fluid treatment at low altitudes to a semikinetic treatment at high altitudes may be an appropriate approach for studying high-latitude ionospheric ion outflows. In this paper we examine the steady state photoelectron-driven polar wind solutions, using the coupled fluid-semikinetic treatment. This model is applied to the polar cap region (latitude of $\geq 80^\circ$) and is divided into three altitudinal zones, which are shown in Figure 1. The lower interface altitude is placed at 800 km altitude here, but in fact the lower interface altitude will vary depending on the non-Maxwellian driving influences in the particular problem. The upper interface altitude is placed at $2 R_E$, as a transition from the collisional semikinetic zone to the collisionless zone. We adopted the MSIS-86 neutral atmosphere for the first (fluid) and second (GSK) regions.

To obtain the initial solution for the plasma bulk parameters in the low-altitude (120–800 km) portion of the solution region, we solved the fluid transport equations using a modified and truncated version of the field line interhemispheric plasma (FLIP) model [Richards and Torr, 1988; Torr *et al.*, 1990], in which the interhemispheric coupling is turned off and replaced by upper boundary conditions given below in equations (7) and (8). A two-stream treatment for photoelectrons is treated in the fluid portion with an initial condition that

The initial conditions for the GSK portion were based on the steady state solution in the absence of photoelectron effects [Su *et al.*, 1995]. The photoelectron distribution at the bottom of the GSK portion was represented as a Maxwellian distribution function, which is a simplified form based on the non-Maxwellian distribution obtained from the two-stream model (Figure 2), with the same average energy and total density flux. The photoelectron densities above 800 km were determined by Liouville mapping Maxwellian photoelectron source distributions from the 800 km altitude and including a cutoff energy at 60 eV. This cutoff energy at 60 eV was obtained from the photoelectron energy spectrum yielded in the two-stream photoelectron model as shown in Figure 2. The cutoff energy at 60 eV is also consistent with Atmosphere Explorer (AE-E) measurements [Lee *et al.*, 1980]. The thermal electron densities were obtained through the quasi-neutrality with the Boltzmann relation, where the thermal electron bulk velocity was assumed to be zero. For closure we iteratively adjusted the electric potential to satisfy the quasi-neutrality condition, which assumed zero potential at 800 km altitude.

The flux tube from 2 to 9 R_E was modeled by using a steady state collisionless semikinetic model, essentially as described by Li *et al.* [1988] and Barakat and Schunk [1983]. One modification here was to allow arbitrary ion distribution functions at the lower boundary instead of only isotropic Maxwellians or bi-Maxwellians. We took the ion distributions at the upper interface altitude from the GSK zone as the lower boundary condition for the collisionless zone, mapping to high-altitude regions using the Liouville theorem, conservation of energy, and conservation of the first adiabatic invariant. The thermal electron densities in the third zone also were obtained from the Boltzmann relation, and the photoelectron densities were again solved with the Liouville mapping method as in the GSK portion.

The plasma must adjust itself such that a large field-aligned current does not develop. There are several possibilities as to how this adjustment could occur: (1) The ionospheric ions could be energized so as to produce upflowing fluxes comparable to those of the photoelectrons. Such high-speed low-altitude outflows were predicted by Tam *et al.* [1995] but have not been observed, (2) Magnetosheath electrons could be drawn down the field line to balance the photoelectron flux, thereby reducing the need for the ionospheric ions to provide the current balance. Typical polar rain particle fluxes in the topside ionosphere lie in the range $10^7 - 10^8 \text{ cm}^{-2} \text{ s}^{-1}$ with energies of about 100 eV [Winningham and Heikkila, 1974], smaller than the observed upward photoelectron fluxes of $10^9 \text{ cm}^{-2} \text{ s}^{-1}$ (varying from 8.6×10^8 for the solar minimum to 1.3×10^9 for the solar maximum at 800 km from our two-stream model), (3) A potential barrier, perhaps in the range 5–40 V, could develop to reflect most of the photoelectrons back to the

ionosphere [Winningham and Gurgiolo, 1982; Pollock *et al.*, 1991; Horwitz *et al.*, 1992].

Because magnetospheric electrons, such as those in the polar rain, could be drawn down the field line to balance the photoelectron flux, and a potential barrier that reflects most of the photoelectrons back to the ionosphere could develop, magnetospheric electrons with a net downward drift are included at the 9 R_E upper boundary. The magnetosheath plasma enters the magnetosphere through merging of the the interplanetary magnetic field with the Earth's magnetic field. The high-energy ions associated with the polar rain were observed and modeled in Plate 1 of Newell *et al.* [1995]. Therefore magnetospheric protons with a net downward drift are also included at the 9 R_E upper boundary. The downward proton and electron densities and temperatures are assumed to be 0.05 cm^{-3} and 100 eV at the top boundary in our simulation.

We solved for the densities for all species via the Liouville mapping technique. For closure we iteratively adjusted the electric potential to satisfy the quasi-neutrality condition,

$$N_{Me}(\phi) + N_{Pe}(\phi) + N_e(\phi) = \quad (6)$$

$$N_{H^+}(\phi) + N_{O^+}(\phi) + N_{Mi}(\phi) \quad (7)$$

where N_{Me} , N_{Pe} , N_e , N_{H^+} , N_{O^+} , and N_{Mi} are the densities for magnetosheath electrons, photoelectrons, thermal electrons, H^+ ions, O^+ ions, and magnetosheath H^+ ions (as functions of the electric potential ϕ), respectively. The electric potential barrier was iteratively adjusted until a currentless condition was achieved across the lower interface altitude at 800 km.

After we solved for the steady state solution for the high-altitude portion, the resulting distribution function solution then provided bulk parameters at the bottom cell of the GSK zone (densities, flow velocities, temperatures, and heat flows). We then used those parameters as boundary conditions for the top cell of the fluid zone and solved the fluid equations below 800 km with upper boundary conditions given by

$$[-kT_i^{5/2} \nabla T_i]_{fluid} = Q_{gsk,i} - (C_{ei} + C_{ni} + C_{ij}) \Delta S \quad (8)$$

$$NV_{fluid,i} = NV_{gsk,i} - (l - q) \Delta S \quad (9)$$

where $Q_{gsk,i}$ and $NV_{gsk,i}$ are the heat flux and density flux given from the bottom of the GSK zone. $NV_{fluid,i}$, T_i , and $kT_i^{5/2}$ are the density flux, temperature, and thermal conductivity of the top of the fluid zone for each species i (H^+ and O^+). C_{ei} , C_{ni} , and C_{ij} are the collisional heating/cooling rates for the ions with electrons, neutrals, and another species of ions, respectively. Since we assumed one cell overlap region between the fluid zone and the GSK zone, ΔS is the length of the overlap cell, and q and l represent the ionization production and loss terms. The heating/cooling terms included in (7) across a single cell in the boundary con-

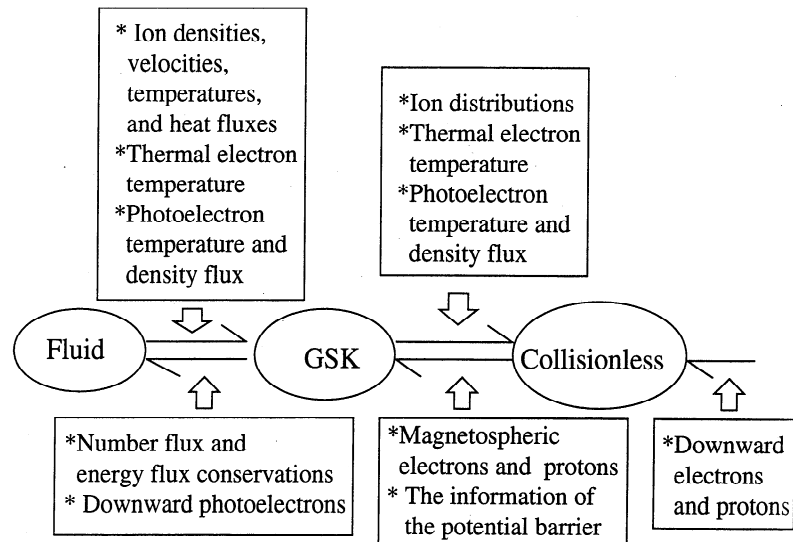


Figure 3. Flowchart of the couple fluid-semikinetic model.

ditions cause a discontinuity of the O^+ heat flux at the interface altitude due to local production in the transition cell.

Much of the upward photoelectron spectrum would be reflected back to the ionosphere by a significant electric potential barrier calculated for the collisionless zone. Since the two-stream treatment was used for the photoelectrons in the fluid zone, the downward photoelectron boundary condition is needed at 800 km. The downward photoelectron energy spectrum is assumed to be a Maxwellian while a potential barrier occurs, usually around 3–5 R_E . The downward photoelectron cutoff energy is described as the potential drop from the fluid boundary to the point where the potential barrier occurs. The high-energy (≥ 100 eV) downward magnetospheric electrons are not included in the fluid zone. When we include penetration of the magnetospheric electrons into the ionosphere, the back scattered electron flux is about $6.6 \times 10^7 \text{ cm}^{-2} \text{ s}^{-1}$ for solar maximum conditions, which is less than the photoelectron flux (about $1.3 \times 10^9 \text{ cm}^{-2} \text{ s}^{-1}$ for solar maximum conditions). It increases the potential barrier at high altitudes by less than 1 V. The secondary electrons created from the polar rain dissipated much of their energy in the ionosphere in nonionizing as well as ionizing collisions. We tentatively suggest that neglecting the magnetospheric electron effects on the ionosphere will not affect the conclusions of this paper significantly.

After again solving for the new bulk parameter profiles for below 800 km we then iterated the GSK injection and solution procedure again with these parameters in the lowest GSK cell, up to the collisionless portion. This procedure was repeated until a satisfactory parameter match of all moment parameters at both interfaces was attained, and we obtained a proper steady state photoelectron-driven polar wind solution for the whole flux tube including the low- and high-altitude re-

gions. Figure 3 shows the summary flowchart of the coupled fluid-semikinetic model.

3. Results

Using the coupled fluid-semikinetic model, we first investigate the steady state photoelectron-driven polar wind for different solar and ionospheric conditions. In this paper we examine the characteristics of the photoelectron-driven polar wind under solar minimum and maximum conditions, referenced to the solar EUV flux at 10.7 cm wavelength, $F_{10.7}$. The solar EUV fluxes are obtained from the EUVAC model [Richards *et al.*, 1994]. The integrated solar flux increases by about a factor of 2–3 from solar minimum to solar maximum. The main effect of increased solar activity on the MSIS model is to increase the neutral temperature which leads to increased neutral densities at F region altitudes. The neutral exospheric temperature increases from 970 K for $F_{10.7} = 90$ to 1370 K for $F_{10.7} = 200$, while the N_2 and O densities increase by about a factor of 3. However, the principal difference of importance here is the change in the photoelectron fluxes from 8.6×10^8 to $1.3 \times 10^9 \text{ cm}^{-2} \text{ s}^{-1}$.

To understand how the photoelectron-driven polar wind could vary with solar zenith angle (day-night asymmetries), we have examined ionospheric conditions with different zenith angles for the ionospheric fluid portion of the treatment. The photoelectron number fluxes and average energies with zenith angles from 0° to 180° at 800 km altitude for both solar minimum and maximum conditions are shown in Figure 4. This figure shows that a significant decrease in photoelectron flux with increasing solar zenith angle occurs from 90° to 115° for both solar minimum and maximum conditions. Thus it would be expected that the largest changes in at least the H^+ polar wind would occur over this range of

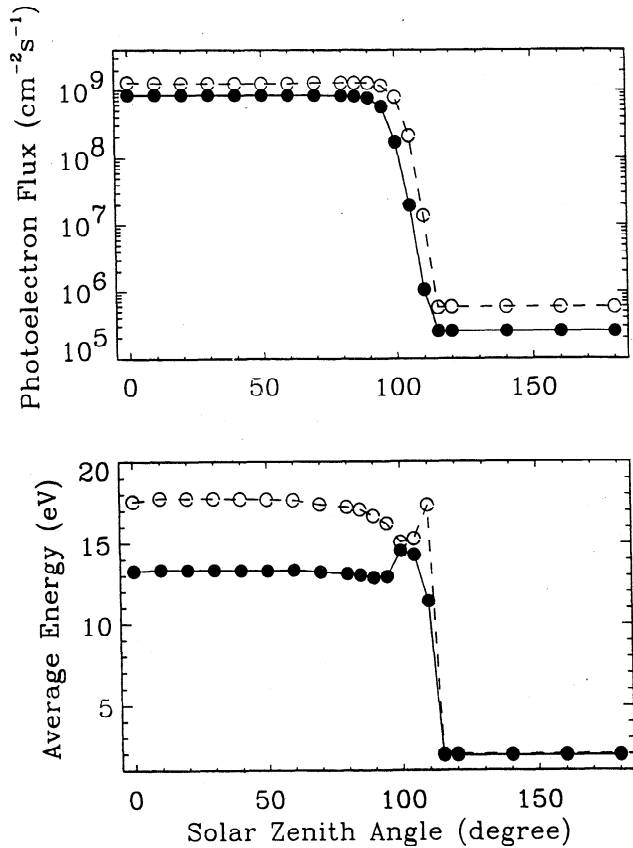


Figure 4. (top) Photoelectron density fluxes and (bottom) average energy with zenith angles from 0° to 180° at 800 km altitude, calculated with the two-stream model in the fluid zone for both solar minimum and maximum conditions, represented by solid lines with solid circles and dashed lines with open circles, respectively.

solar zenith angles, as might occur near sunset or sunrise. The following results are presented for the sunlit ionosphere, taken here to be for 60° zenith angle for solar minimum, and 65° for solar maximum.

3.1. Solar Minimum Case

For solar minimum conditions the relevant parameter for the lower ionosphere portion is $F_{10.7} = 90$ (10^{-22} $\text{W m}^{-2} \text{ Hz}^{-1}$). A 13.2 eV characteristic photoelectron temperature and $8.6 \times 10^8 \text{ cm}^{-2} \text{ s}^{-1}$ for the photoelectron flux are obtained at 800 km from the two-stream photoelectron model. The calculated photoelectron energy spectrum (solid line) at 800 km from the fluid zone solution is shown in Figure 2.

To obtain a solution satisfying both zero current and quasi-neutrality conditions, the model iteratively modifies the electric potential until charge neutrality is achieved. This process yields multiple solutions. One such solution has a relatively small potential drop (< 5 V). This solution, however, does not satisfy the currentless condition because the potential drop along the field line is insufficient to reflect enough of the photoelec-

trons back toward the ionosphere. However, another solution yields, for this case, a 40 V potential drop, much of which occurs in a sharp discontinuity at $3.4 R_E$ altitude, and the combination of fluxes for all species leaves a negligible residual field-aligned current of $0.02 \mu\text{A m}^{-2}$ out of the ionosphere. Hence such a solution can effectively satisfy both the conditions of charge neutrality and zero current. It results in downward electron fluxes into the ionosphere of $6.4 \times 10^7 \text{ cm}^{-2} \text{ s}^{-1}$, consistent with polar rain measurements [Winningham and Heikkila, 1974]. Figure 5 shows ion densities in the first panel, electron densities in the second panel, ion parallel bulk flow speeds in the third panel, and the electric potential in the fourth panel for the range 120 km to $9 R_E$ altitude. When the 40 V potential drop occurs at $3.4 R_E$ altitude, both H^+ and O^+ ion densities decrease by about a factor of 10, and the O^+ bulk velocity increases from 2.5 to 21 km s^{-1} while the H^+ velocity increases from 25 to 84 km s^{-1} . The thermal electrons are totally reflected back to the ionosphere by the potential drop, as is much of the photoelectron spectrum.

To illustrate the differences between the photoelectron-driven polar wind solution and the baseline polar wind in the absence of photoelectrons and magnetospheric populations, Figure 6 shows a comparison between the photoelectron-driven polar wind results and baseline polar wind results for solar minimum conditions. Below the potential layer (in the photoelectron included case) the two results are similar, except that the O^+ density decreases by about a factor of 10 above the transition region when photoelectron effects are neglected. In the case with photoelectron effects, both H^+ and O^+ ions are accelerated by the large potential drop. The ion density decreases with increasing velocity, since the number flux remains constant along the flux tube. However, the O^+ velocity is less than 3 km s^{-1} , and H^+ velocity is less than 30 km s^{-1} , while the potential drop is less than 5 V in the case in which photoelectron effects are neglected. The comparison indicates a strong influence by photoelectrons and magnetospheric populations on the polar wind at high altitudes ($\geq 3 R_E$) but not at low altitudes.

Since the fluid and semikinetic codes are coupled at 800 km altitude with density flux and heat flux conservation conditions, we expect to match all moment parameters across the interface. Figure 7 shows an expanded version of the density, bulk velocity, density flux, temperature, and heat flux profiles in the 120–5000 km altitude regions and across the lower interface altitude (800 km). Above 1000 km altitude the density flux and heat flux remain almost constant. A very good match across the boundary was obtained for densities, flow speeds, density fluxes, temperatures, and heat fluxes for the local ions (the O^+ heat flux has a discontinuity due to local production in the overlap cell, as we discussed earlier). The O^+ density peak is at about 250 km altitude, while the H^+ density peak is at

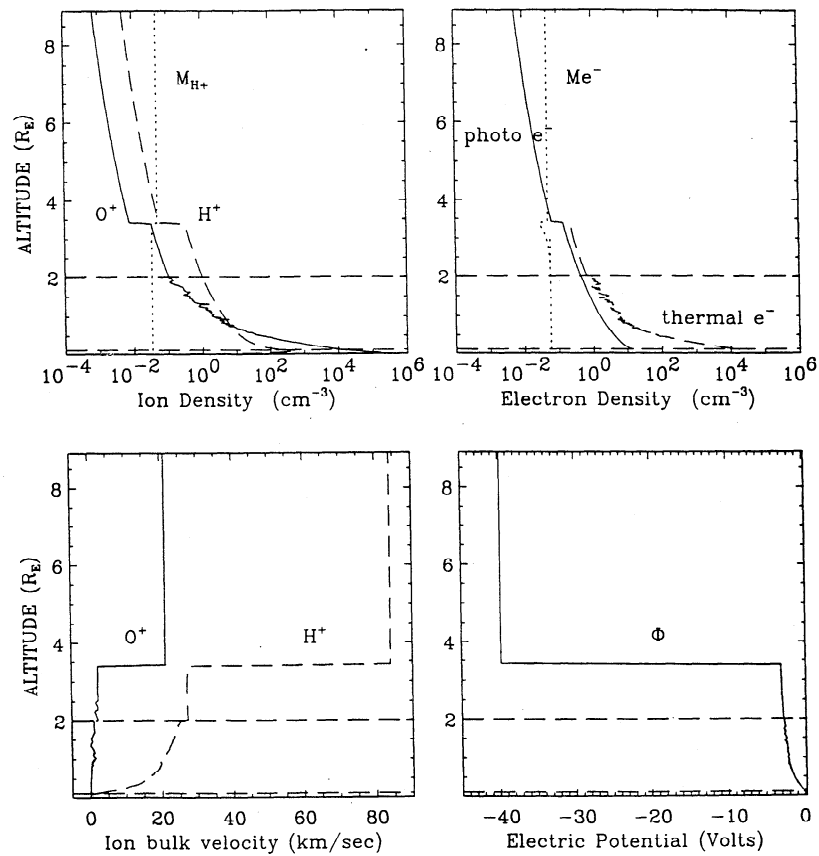


Figure 5. Steady state results for solar minimum conditions. Ion densities, electron densities, ion flow velocities, and electron potential are shown in the first, second, third, and fourth panels, respectively. Solid and dashed lines represent O^+ and H^+ profiles in the first and third panels, and the dotted line represents the magnetosheath H^+ ion density in the first panel. In the second panel the solid, dashed, and dotted lines represent the photoelectron, thermal electron, and downward magnetosheath electron densities, respectively. The two horizontal long-dashed lines of each plot represent the lower (800 km) and upper ($2 R_E$) interface boundaries.

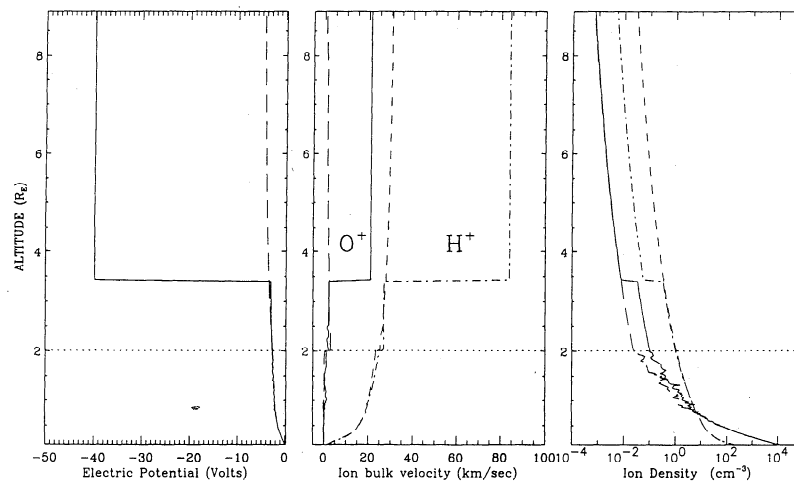


Figure 6. Comparison between the photoelectron-driven polar wind results (W) and the results obtained while neglecting photoelectrons as well as magnetospheric populations (WO) for solar minimum conditions. (left) Electric potentials. Solid and long-dashed lines represent W and WO cases. (center) Ion bulk velocities and (right) densities. Solid and dot-dashed lines represent O^+ and H^+ profiles in the W case, and the long-dashed and short-dashed lines represent the O^+ and H^+ profiles in the WO case. The horizontal dotted lines represent the upper interface boundary.

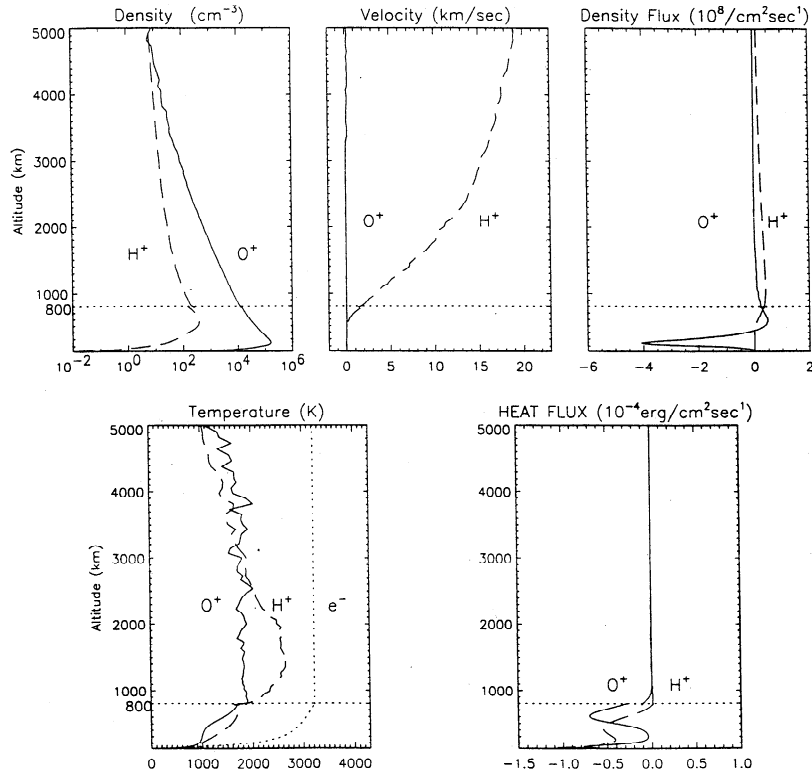


Figure 7. Ion density, bulk velocity, density flux, temperature, and heat flux profiles from 120 to 5000 km altitude, and across the interface altitude (800 km here), for solar minimum conditions. The solid and dashed lines represent the O^+ and H^+ ion profiles, respectively. The horizontal dotted lines indicate the lower interface boundary.

550 km. Above the density peaks, both ion densities decrease with increasing altitude; the H^+ ions accelerate from 2 km s^{-1} at 800 km to 19 km s^{-1} at 5000 km altitude, but the O^+ ion velocity is only about 1 km s^{-1} at 5000 km.

The H^+ (top two rows) and O^+ (bottom two rows) distribution contours in phase space in the GSK zone are shown in Figure 8. The circular H^+ and O^+ distribution function contours at the lowest altitude just above (800 km) the GSK region are indicative of Maxwellians and tend to validate our use of a fluid treatment, which presumes such a description up to 800 km altitude. On the other hand, it is evident that the H^+ ion distribution functions depart from simple drifting Maxwellians above 2000 km or so, validating the importance of utilizing a kinetic treatment for the higher-altitude treatment. In the transition region (1300–5000 km altitude) the H^+ distribution functions contain significant downward parallel heat fluxes, due to the competing effects of the ambipolar electric field acceleration of H^+ and collisional drag with O^+ , which lead to these non-Maxwellian H^+ velocity distributions.

3.2. Solar Maximum Case

For the solar maximum condition the relevant parameter for the lower ionosphere portion is $F_{10.7} = 200$

($10^{-22} \text{ W m}^{-2} \text{ Hz}^{-1}$). A 17.7 eV characteristic photoelectron temperature and $1.3 \times 10^9 \text{ cm}^{-2} \text{ s}^{-1}$ for the photoelectron flux are obtained at 800 km by the two-stream photoelectron model. The photoelectron energy spectrum (dashed line) at 800 km is shown in Figure 2. Multiple solutions for the potential profile were obtained, but again we consider only the solutions that satisfied both the conditions of charge neutrality and nearly zero current. In this case a 46 V potential drop between the ionosphere and magnetosphere was attained with a significant jump at $5.2 R_E$ altitude. The magnetospheric electron flux into the ionosphere is $7.5 \times 10^7 \text{ cm}^{-2} \text{ s}^{-1}$, and the combination of fluxes for all species leaves a small residual field-aligned current of $0.01 \mu\text{A m}^{-2}$ out of the ionosphere. Ion densities, electron densities, ion parallel bulk flow speeds, and electric potential are shown in the first, second, third, and fourth panels, respectively, of Figure 9 for 120 km to $9 R_E$ altitude. When the potential barrier (46 V) occurs at $5.2 R_E$, ion and photoelectron densities decrease significantly while the thermal electrons are totally reflected back to the ionosphere. The O^+ ions accelerate to a bulk velocity of 22.5 km s^{-1} , while the H^+ ion velocity increases to 90 km s^{-1} .

To illustrate the differences between the photoelectron-driven polar wind solution and the baseline po-

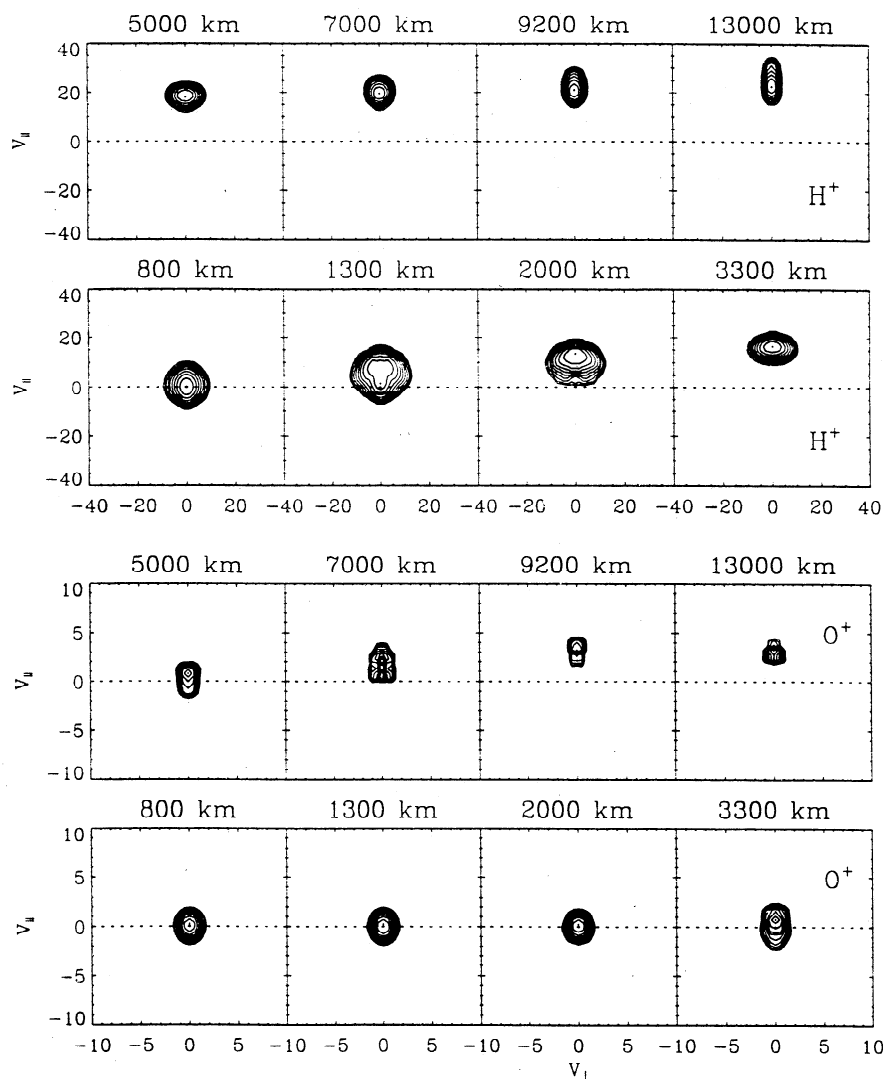


Figure 8. H^+ and O^+ velocity distribution contours at different altitudes within the GSK zone for solar minimum conditions. The H^+ distribution contours are shown in the top two rows; the velocity ranges are from -40 to 40 km s^{-1} in both the parallel and perpendicular directions. The O^+ contours are shown in the bottom two rows with corresponding velocity ranges from -10 to 10 km s^{-1} in both directions.

lar wind solution in the absence of photoelectrons and magnetospheric populations, Figure 10 shows a comparison between the photoelectron-driven polar wind results and baseline polar wind results for solar maximum conditions. Again the comparison demonstrates a strong influence by photoelectrons and magnetospheric populations on the polar wind at high altitudes but not at low altitudes.

To illustrate the differences in the solutions for solar minimum and solar maximum conditions, Figure 11 displays the profiles for the electric potential, ion densities, and ion bulk velocities for both solar minimum and maximum conditions. The total potential drop between the ionosphere and the magnetosphere in the first panel in Figure 11 is 40 V for solar minimum and 46 V for solar maximum. This difference is due to the fact that the escaping photoelectron flux is about 17 times

greater than the precipitating magnetospheric electron flux for the solar maximum condition, while it is about 13 times greater for the solar minimum condition. The ion flow speeds increase and densities decrease with this increasing potential drop between the two cases.

A comparison of ion flow speeds and densities for these solar minimum and maximum conditions is shown in the center and right panels in Figure 11. O^+ is the dominant ion species at low altitudes (≤ 5000 km altitude), and H^+ becomes the dominant ion species at higher altitudes ($\geq 1 R_E$ altitude). The ion bulk velocities exhibit no significant differences below the potential layer between the solar maximum and minimum cases (only H^+ ions have a slightly higher velocity in the minimum case than in the maximum case), while O^+ densities are 5 times larger in the maximum case than in the minimum case, and H^+ densities are only

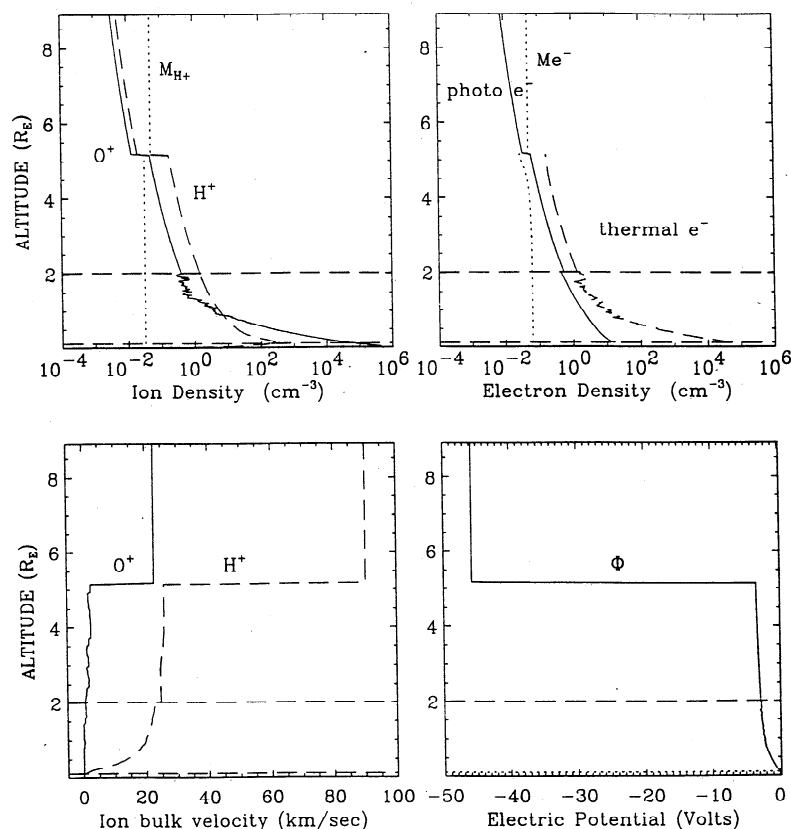


Figure 9. Steady state results for solar maximum. The ion densities, electron densities, ion flow velocities, and electron potential are shown in the first, second, third, and fourth panels, respectively. The solid and dashed lines represent O^+ and H^+ profiles, respectively, in the first and third panels, and the dotted line represents the magnetosheath H^+ ion densities in the second panel. In the second panel the solid, dashed, and dotted lines represent the photoelectron, thermal electron, and magnetosheath electron densities, respectively. The two horizontal long-dashed lines of each plot represent the lower and upper interface boundaries.

about twice as large at altitudes below the significant potential drop. The potential layers accelerate the ionospheric ions at high altitudes (above $3 R_E$ altitude) but not at low altitudes (e.g., <3000 km) in our results.

4. Discussion

Our results show that for both the solar minimum and maximum cases a magnetospheric plasma density of 0.05 cm^{-3} was required to balance the photoelectron current that we used. This finding is consistent with observations from the plasma mantle [Shodhan *et al.*, 1996] but is low in comparison with those for the magnetosheath [Sibeck and Gosling, 1996]. This condition results in magnetospheric electron fluxes into the ionosphere of about $6\text{--}7 \times 10^7 \text{ cm}^{-2} \text{ s}^{-1}$, consistent with polar rain measurements [Winningham and Heikkila, 1974]. The electric potential layer is computed to be 46 V at solar maximum and 40 V at solar minimum. The potential layer accelerates O^+ ions to 21 (22.5) km s^{-1} and H^+ ions to 84 (90) km s^{-1} for solar minimum (maximum) conditions.

We also examined cases with magnetospheric electron fluxes increased to $6.5 \times 10^8 \text{ cm}^{-2} \text{ s}^{-1}$ and a density of 2.2 (1.3) cm^{-3} for solar minimum (maximum) conditions to obtain a near-currentless condition, although these fluxes are much higher than observations appear to support. The results are shown in Figure 12 for solar minimum conditions and Figure 13 for maximum conditions. In these two cases the upper interface altitude is at $2.75 R_E$, which is $3.75 R_E$ geocentric distance in the figures. For such cases the potential drops were sharply reduced to 8.3 V at solar minimum and 16.2 V at solar maximum. The ion parallel bulk velocities in these cases were 30 (50) km s^{-1} for H^+ ions and 8 (12) km s^{-1} for O^+ ions at high altitudes for solar minimum (maximum) conditions.

From our simulation results the ion acceleration depends on the potential drop, and the potential layer is primarily determined by the ionospheric photoelectron flux and magnetospheric electron flux. To illustrate the effect of variations in the magnetosheath plasma density, Figure 14 shows the potential layer versus the magnetospheric electron density for both solar mini-

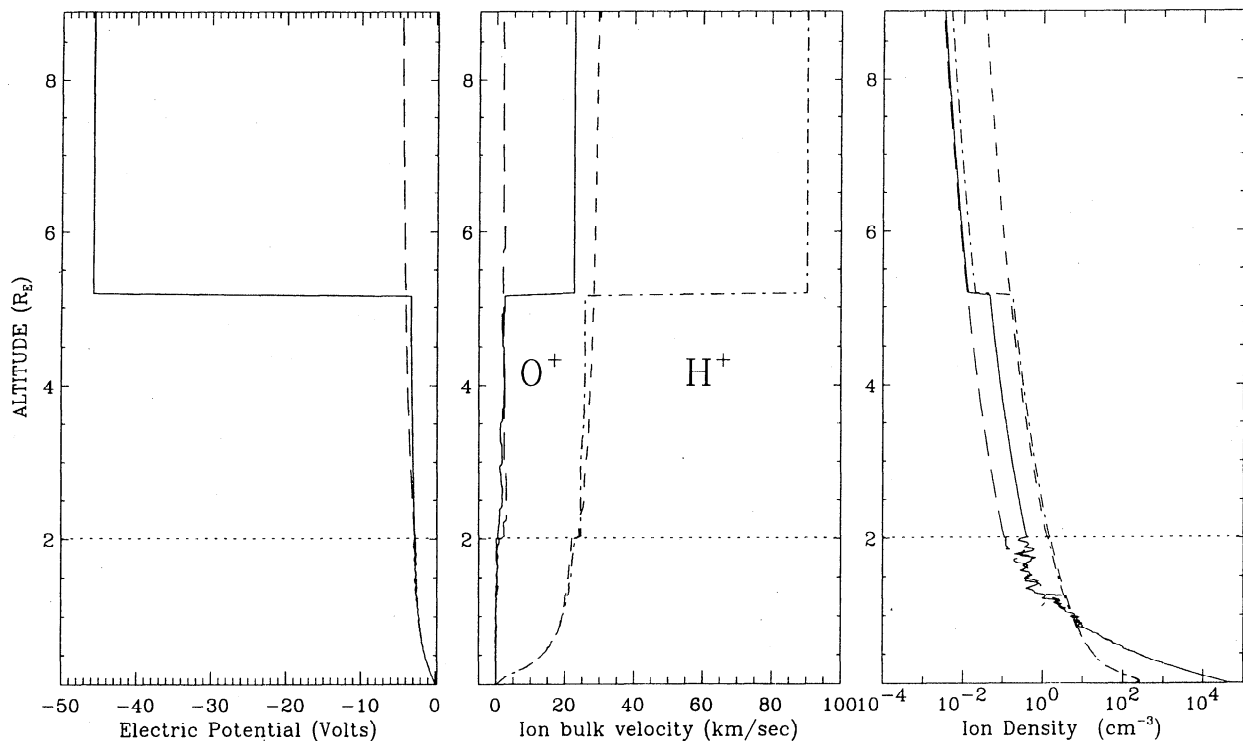


Figure 10. Comparison between the photoelectron-driven polar wind results (W) and the results obtained while neglecting photoelectrons as well as magnetospheric populations (WO) for solar maximum conditions. (left) Electric potentials; the solid and long-dashed lines represent W and WO cases. (center) Ion bulk velocities and (right) densities. The solid and dot-dashed lines represent O^+ and H^+ profiles in the W case, and the long-dashed and short-dashed lines represent the O^+ and H^+ profiles in the WO case. The horizontal dotted lines indicate the upper interface boundary.

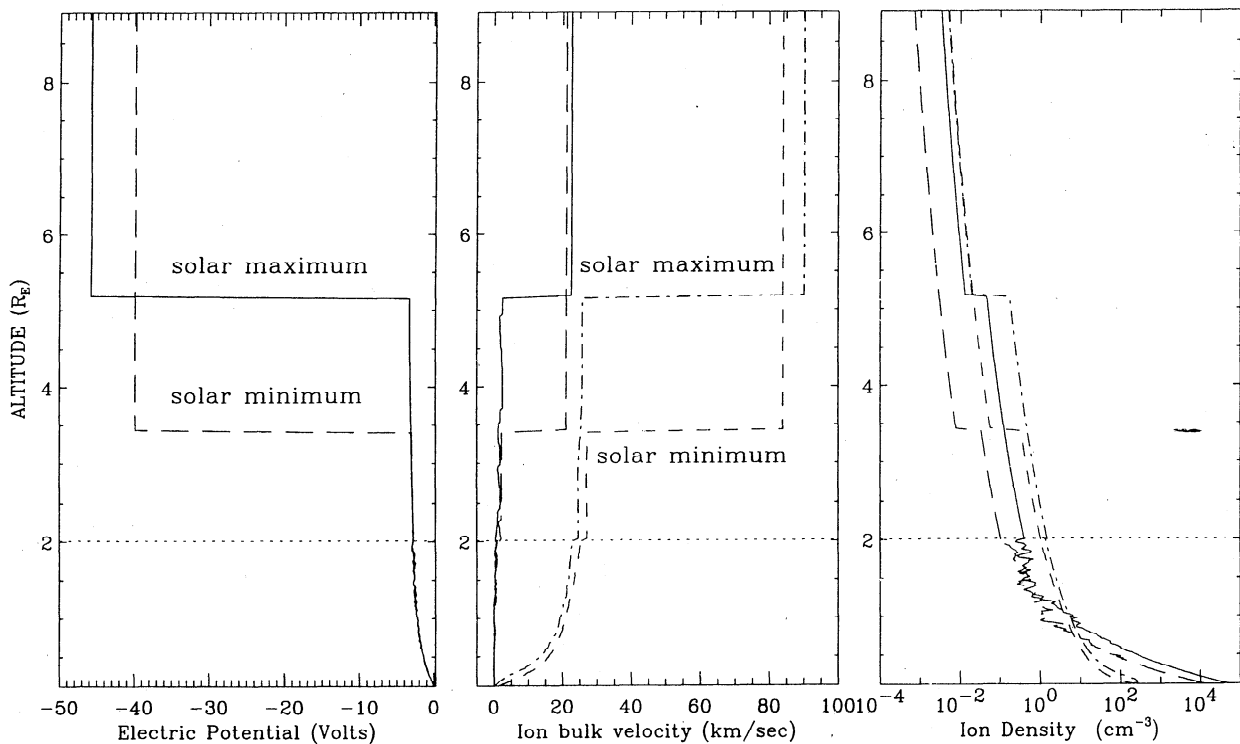


Figure 11. Comparison of solar minimum and maximum results. (left) Electric potentials; the solid and long-dashed lines represent the solar maximum and minimum results. (center) Ion bulk velocities and (right) densities. The solid and dot-dashed lines represent O^+ and H^+ profiles at solar maximum, and the long-dashed and short-dashed lines represent the O^+ and H^+ profiles at solar minimum. The horizontal dotted lines represent the upper interface boundary.

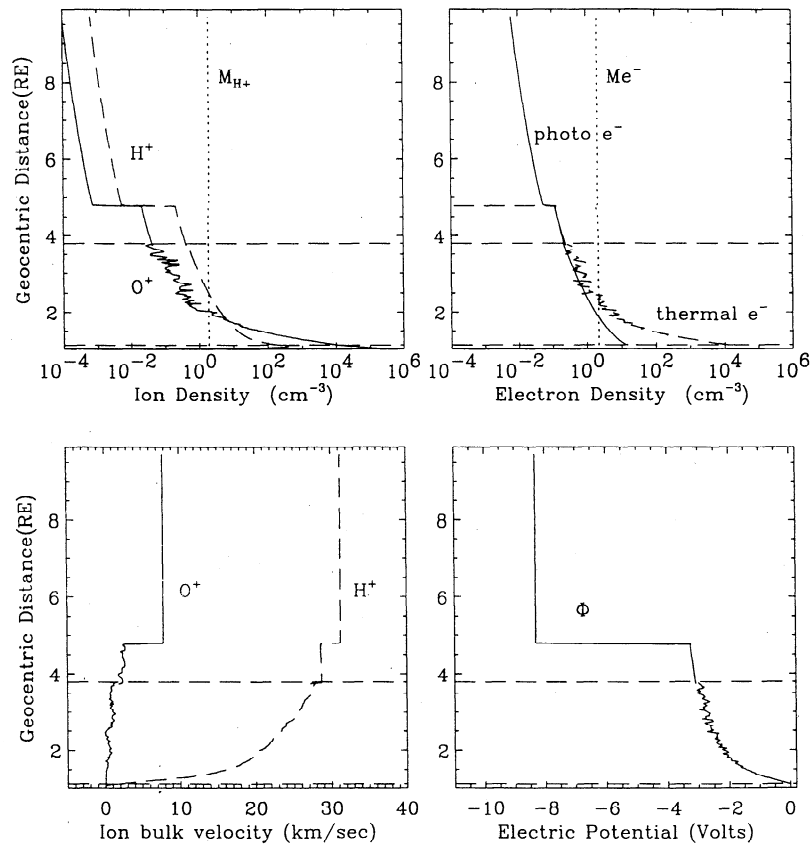


Figure 12. Photoelectron-driven polar wind results with 2.2 cm^{-3} downward magnetospheric electron density for solar minimum conditions. The format of the plot is similar to that of Figure 5, except the vertical axis is in units of geocentric distance.

num and maximum conditions. These quantities are shown in Table 1 as well. The potential layer decreases with increasing magnetospheric electron flux when the ionospheric conditions are the same and the magnetospheric electron density increases from 0.05 to 2 cm^{-3} . This result indicates that the potential barrier develops because the flux of electrons from the magnetosphere

to the ionosphere (as seen in the polar rain) is insufficient to balance the injected photoelectron flux from the ionosphere.

Observations of such photoelectron distributions in the topside ionosphere by *Winningham and Heikkila* [1974] and *Winningham and Gurgiolo* [1982] have led these authors to conclude that large-scale electrostatic

Table 1. Potential Layer Versus Magnetospheric Ion Density for Solar Minimum and Maximum

N_{ME}, cm^{-3}	Solar Minimum ^a		Solar Maximum ^b	
	$F_{ME}, \text{cm}^{-2} \text{s}^{-1}$	Φ_E, V	$F_{ME}, \text{cm}^{-2} \text{s}^{-1}$	Φ_E, V
0.05	6.44×10^7	39.8	7.51×10^7	45.7
0.10	1.19×10^8	36.5	1.35×10^8	40.9
0.50	3.57×10^8	22.0	4.36×10^8	26.4
1.00	5.16×10^8	15.3	6.27×10^8	18.9
1.50	5.82×10^8	11.4	7.30×10^8	14.6
2.00	6.24×10^8	8.5	7.90×10^8	11.7

N_{ME} is the magnetospheric electron density, F_{ME} is the magnetospheric electron number flux, and Φ_E is the potential drop.

^a $F_{10.7} = 90$, solar zenith angle = 60° , photoelectron average energy = 13.35 eV , and photoelectron number flux = $8.52 \times 10^8 \text{ cm}^{-2} \text{s}^{-1}$.

^b $F_{10.7} = 200$, solar zenith angle = 65° , photoelectron average energy = 17.7 eV , and photoelectron number flux = $1.3 \times 10^9 \text{ cm}^{-2} \text{s}^{-1}$.

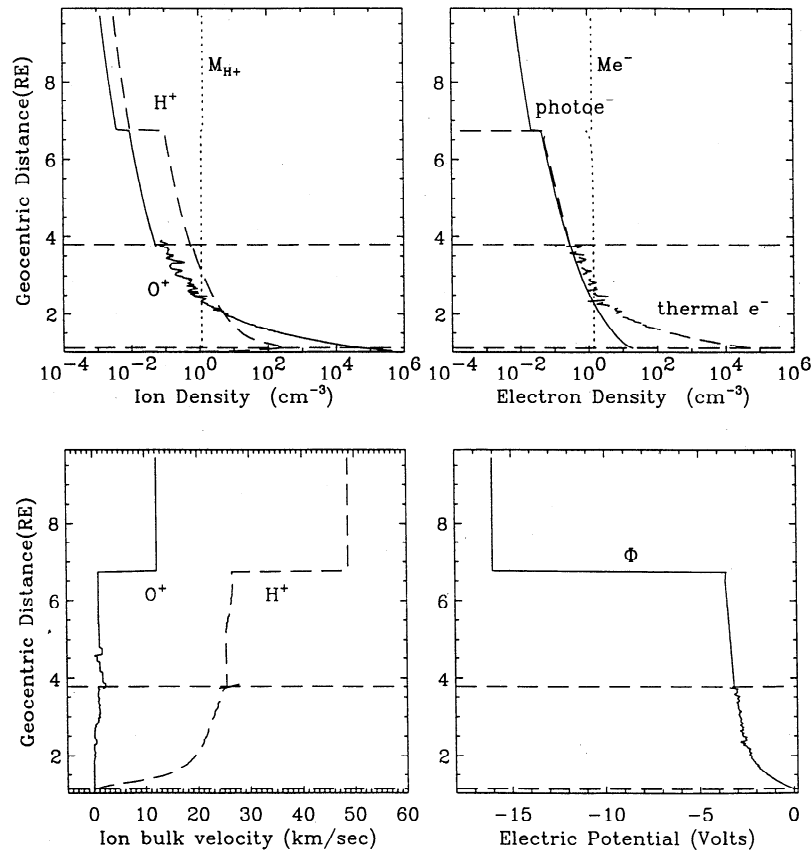


Figure 13. Photoelectron-driven polar wind results with 1.3 cm^{-3} downward magnetospheric electron density for solar maximum conditions. The format of the plot is similar to that of Figure 9, except the vertical axis is in units of geocentric distance.

potential drops exist above the spacecraft (ISIS 1 and DE 2, respectively) along polar magnetic field lines connected to regions of photoelectron production. Further, more detailed, survey observations of atmospheric photoelectrons from DE 1 [Pollock *et al.*, 1991; Horwitz *et al.*, 1992] have indicated that a field-aligned potential drop of the order of 5–40 V may exist above the low altitude of the DE 2 spacecraft (about 1000 km), particularly toward the dayside. Such electrostatic potential drops reflect electrons back toward Earth, and positive ions entering the potential drop region from below are accelerated outward, away from the ionosphere. The average flow speeds of the O^+ and H^+ ions in the polar cap at altitudes up to $1 R_E$ do not suggest large potential differences (5 V or more) between the F region and an altitude of $1 R_E$ [e.g., Chandler *et al.*, 1991; Abe *et al.*, 1993a]. This observation may be contrasted with the kinetic collisional calculations by Tam *et al.* [1995] which have suggested that significant potential drops (about 10 V) would occur below 2000 km altitude and O^+ and H^+ velocities of 10–40 km s^{-1} near 600 km altitude. A direct comparison of our new results on the photoelectron-driven polar wind with the results by Tam *et al.* [1995] from 500 to 12,000 km altitude is shown in Figure 15. The lines present our results for solar maximum, and the symbols are scaled from the

results by Tam *et al.* [1995]. Below 12,000 km altitude the potential drop is less than 3 V in our results. Our modeling results and those of Wilson *et al.* [1997] indicate that the large potential drops of the order of 40 V or higher may occur, but at high altitudes, above $3 R_E$. Such potential layers would accelerate the ionospheric ions at these high altitudes ($\geq 3 R_E$) which seem consistent with observations, but our model does not predict the low-altitude (≤ 3000 km) ion acceleration suggested by Tam *et al.* [1995].

Barakat and Schunk [1983], using the steady state collisionless semikinetic model, concluded that energetic O^+ outflow occurs at high altitude when the electron temperature is high (10,000 K), but not with 3000 K electron temperature. Later, Barakat and Schunk [1984a] included effects of hot electrons, polar rain, polar showers, and polar squall and further studied the polar wind with a semikinetic model for the altitude region 4500 km to $10.5 R_E$. When the hot/cold electron temperature ratio was greater than 100 and the hot/cold density ratio was greater than 0.01, a “double-layer” potential barrier occurred, which reflected the cold ionospheric electrons and prevented them from attaining higher altitudes. We compare our results with the results of Barakat and Schunk [1983, 1984a] in Figure 16, where the H^+ densities, O^+ densities, H^+ ve-

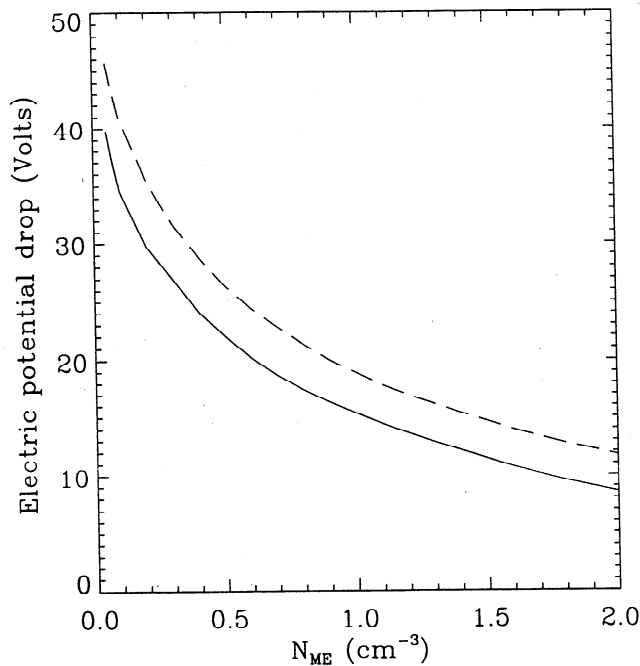


Figure 14. Potential drop versus magnetospheric electron density. The solid and long-dashed lines represent the solar minimum and maximum conditions, respectively.

locities, and O^+ velocities are shown in the first, second, third, and fourth panels, respectively. The diamonds are scaled from the original case, which was assumed 3000 K for the thermal electron temperature, and the triangles are scaled from the case in which Barakat and Schunk [1983] assumed the electron temperature to be 10,000 K. The asterisks with solid lines are scaled from the case with a hot/cold electron temperature ratio of 100, while the hot/cold electron density ratio is 0.01 [Barakat and Schunk, 1984a]. The solid and long-dashed lines present our photoelectron-driven polar wind results and the results which obtained by neglecting photoelectrons as well as magnetospheric populations, respectively. Both H^+ and O^+ densities at 4500 km altitude from the Barakat and Schunk [1983, 1984a] papers are about 1–2 orders of magnitude larger than the densities were from our results, while the velocities are comparable. Barakat and Schunk [1983, 1984a] assumed ion fluxes of about $1 \times 10^8 \text{ cm}^{-2} \text{ s}^{-1}$ at their lower boundary, which is higher than the total ion flux from our fluid calculation, which at 800 km altitude is of the order of 10^7 in the polar cap region. It is interesting to note that the Barakat and Schunk [1984a] results contain a potential layer discontinuity similar to the potential discontinuity in our own photoelectron-driven polar wind results. For higher hot electron temperature and a greater percentage of hot electrons [Barakat and Schunk, 1984a] there is a sharp transition, which corresponds to a contact surface between the hot and cold electrons. They conclude that the “double layer” acts to reflect the cold ionospheric electrons and retard the

escaping photoelectrons. From our results it is clear that the potential barrier occurs because the flux of electrons from the magnetosphere to the ionosphere is insufficient to balance the injected photoelectron flux from the ionosphere.

Yau *et al.* [1985] concluded that the acceleration altitude of O^+ upflowing ions is modulated by the atmospheric scale height, which increases with increasing solar activity (EUV flux), but there were no significant solar cycle variations in the occurrence of H^+ upflowing ions observed by the DE 1 satellite (energy ion composi-

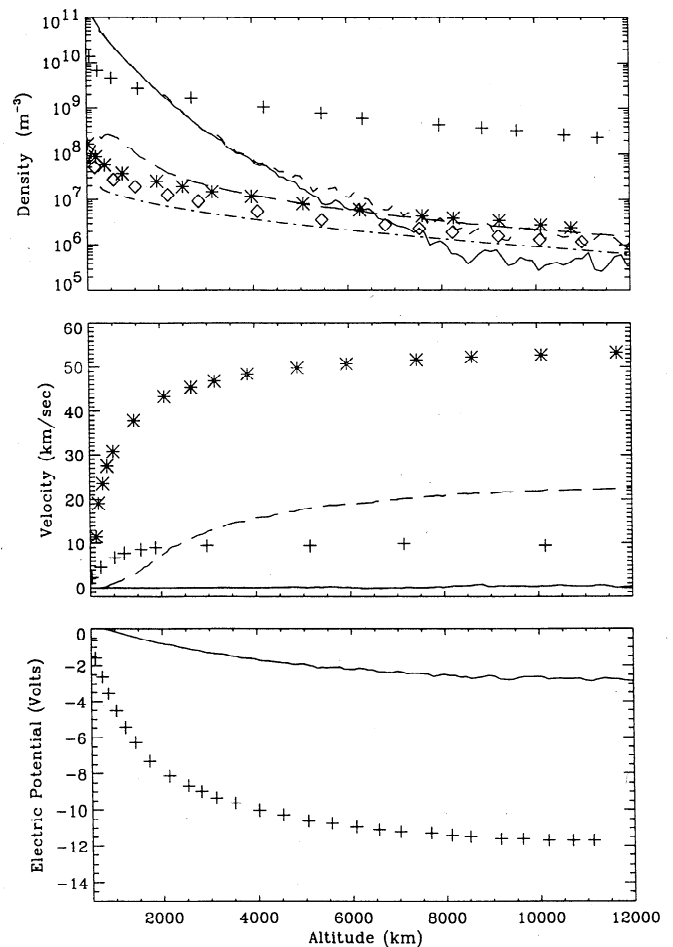


Figure 15. Comparison of our photoelectron-driven polar wind results with results by Tam *et al.* [1995]. (top) Densities, (middle) velocities, and (bottom) electric potentials from 500 to 12,000 km altitude. (top) The plus signs, asterisks, and diamonds are scaled from O^+ , H^+ , and photoelectron density profiles in their Figure 2. (The thermal electron profile overlaps with the O^+ density profile.) The solid, long-dashed, dot-dashed, and short-dashed lines represent O^+ , H^+ , photoelectron, and thermal electron profiles from our solar maximum results. (middle) The plus and asterisks signs are scaled from O^+ and H^+ velocity profiles from their Figure 3. The solid and long-dashed lines represent O^+ and H^+ velocity profile from our results. (bottom) The plus signs are scaled from their electric potential profile in Figure 1, and the solid line represents our potential profile.

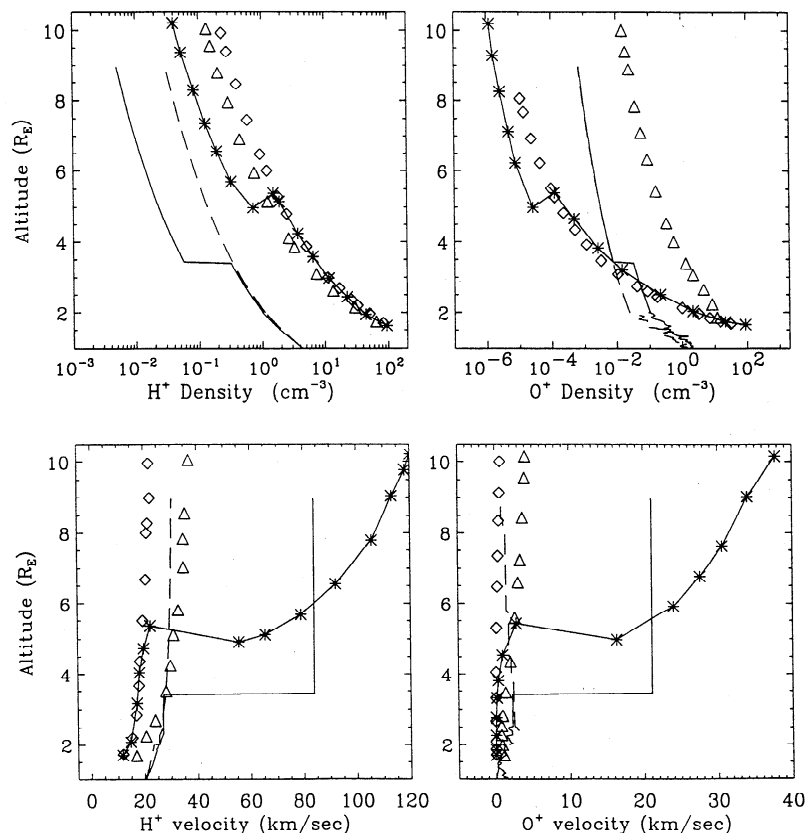


Figure 16. Comparison of our present results with those of semikinetic polar wind studies by Barakat and Schunk [1983, 1984a]. The H^+ and O^+ densities are shown in the top two panels, and velocities are shown in the bottom two panels from 1 to $10.5 R_E$ altitude. The diamonds are scaled from profiles with 3000 K electron temperature, and the triangles are scaled from profiles with 10,000 K electron temperature in Figure 1 of Barakat and Schunk [1983]. The asterisks are scaled from the profiles with suprathermal electron population in the paper of Barakat and Schunk [1984a], with hot and cold electron density ratio of 0.01 and temperature ratio of 100. The solid lines represent our results with photoelectron effects for the solar minimum, and the long-dashed lines represent our results without photoelectrons and magnetospheric particles.

tions spectrometer) in the high-altitude (8000–23,000 km) auroral and polar cap ionosphere-magnetosphere. Chandler *et al.* [1991] studied the solar cycle variations of polar ion outflows by DE 1 retarding ion mass spectrometer measurements at altitudes between 1000 and 4000 km. The O^+ density increased with increased $F_{10.7}$ at all altitudes. The increase (about a factor of 2 in their Figure 10) is consistent with an increase in the solar EUV flux, which is assumed to accompany a long-term increase in the $F_{10.7}$ flux. There was no significant change in the H^+ density (their Figure 11). They also indicated that there were few observations from the periods when $F_{10.7} > 200$ and fewer still for $F_{10.7} < 100$. Our simulation results indicate that the O^+ and H^+ densities increase with increased $F_{10.7}$ for altitudes below $3 R_E$. For an $F_{10.7}$ increase from 90 to 200 the increase is about a factor of 5 for O^+ but only about a factor of 2 for H^+ . More recently, Moore *et al.* [1997] and Su *et al.* [1997] have reported preliminary polar wind H^+ flow velocities in the range 20–80 km s⁻¹ and O^+ flows of 5–25 km s⁻¹ along the local magnetic field

from the Thermal Ion Dynamics Experiment (TIDE) on the POLAR spacecraft at very high altitudes (about $8 R_E$). Our photoelectron-driven polar wind results are comparable with the highest velocities of these ion outflow POLAR/TIDE observations. The average O^+/H^+ velocity ratio is about 2/5 from TIDE observation at high altitude ($8 R_E$), which suggests the importance of comparable energy gains (O^+/H^+ velocity ratio = 1/4). In our photoelectron-driven polar wind results, both O^+ and H^+ ions gain the same energy from the potential layer at high altitudes, compatible with the TIDE observations.

The early kinetic polar wind models including escaping photoelectrons by Lemaire [1972] adopted boundary conditions at 950 km altitude. The recent semikinetic models of the photoelectron-driven polar wind by Tam *et al.* [1995] and Wilson *et al.* [1997] have started from a boundary of 500 km altitude. For all the early models the lower boundary conditions were assumed as input parameters, without self-consistent and direct calculation. However, ionospheric ions and

electrons are produced in large part by photoionization of the neutral atmosphere below 500 km altitude. Therefore our coupled fluid-semikinetic model, which incorporates the lower-altitude sources of both the ionospheric thermal plasmas and the suprathermal photoelectrons, is suitable for self-consistently investigating the photoelectron-driven polar wind. As in this paper, we can examine the differences between solar minimum and maximum conditions, as well as different solar zenith angle cases for different ionospheric conditions.

Acknowledgments. This work was supported in part by NASA grants NAGW-1554 and NAGW-4455, NSF grants ATM-9301024, ATM-9402310, and ATM-9523786, and NASA cooperative agreement NCC8-65 to The University of Alabama in Huntsville.

The Editor thanks J. M. Grebowsky and R. Link for their assistance in evaluating this paper.

References

- Abe, T., B. A. Whalen, A. W. Yau, R. E. Horita, S. Watanabe, and E. Sagawa, EXOS D (Akebono) suprathermal mass spectrometer observations of the polar wind, *J. Geophys. Res.*, **98**, 11,191, 1993a.
- Abe, T., B. A. Whalen, A. W. Yau, S. Watanabe, E. Sagawa, and K. I. Oyama, Altitude profile of the polar wind velocity and its relationship to ionospheric conditions, *Geophys. Res. Lett.*, **20**, 2825, 1993b.
- Axford, W. I., The polar wind and the terrestrial helium budget, *J. Geophys. Res.*, **73**, 6855, 1968.
- Banks, P. M., and T. E. Holzer, The polar wind, *J. Geophys. Res.*, **73**, 6846, 1968.
- Banks, P. M., and T. E. Holzer, Features of plasma transport in the upper atmosphere, *J. Geophys. Res.*, **74**, 6304, 1969.
- Barakat, A. R., and R. W. Schunk, O^+ ions in the polar wind, *J. Geophys. Res.*, **88**, 7887, 1983.
- Barakat, A. R., and R. W. Schunk, Effect of hot electrons on the polar wind, *J. Geophys. Res.*, **89**, 9771, 1984a.
- Barakat, A. R., and R. W. Schunk, O^+ charge exchange in the polar wind, *J. Geophys. Res.*, **89**, 9835, 1984b.
- Barakat, A. R., R. W. Schunk, T. E. Moore, and J. H. Waite, Ion escape fluxes from the terrestrial high-latitude ionosphere, *J. Geophys. Res.*, **92**, 12,255, 1987.
- Bauer, S. J., The structure of the topside ionosphere, in *Electron Density Profiles in Ionosphere and Exosphere*, edited by J. Frihagen, pp. 387-397, North-Holland, New York, 1966.
- Brown, D. G., G. R. Wilson, J. L. Horwitz, and D. L. Gallagher, "Self-consistent" production of ion conics on return current region auroral field lines: A time-dependent, semikinetic model, *Geophys. Res. Lett.*, **18**, 1841, 1991.
- Brown, D. G., P. G. Richards, J. L. Horwitz, and G. R. Wilson, Semikinetic simulation of effects of ionization by precipitating auroral electrons on ionospheric plasma transport, in *Cross-Scale Coupling in Space Plasmas*, *Geophys. Monogr. Ser.*, vol. 93, edited by J. L. Horwitz, N. Singh, and J. L. Burch, p. 97, AGU, Washington, D. C., 1995.
- Chandler, M. O., J. H. Waite Jr., and T. E. Moore, Observations of polar ion outflow, *J. Geophys. Res.*, **96**, 1421, 1991.
- Demars, H. G., and R. W. Schunk, Solution to bi-Maxwellian transport equations for SAR-arc conditions, *Planet. Space Sci.*, **34**, 1335, 1986.
- Demars, H. G., and R. W. Schunk, Comparison of solutions to bi-Maxwellian and Maxwellian transport equations for subsonic flows, *J. Geophys. Res.*, **92**, 5969, 1987.
- Dessler, A. J., and F. C. Michel, Plasma in the geomagnetic tail, *J. Geophys. Res.*, **71**, 1421, 1966.
- Ganguli, S. B., Plasma transport in the auroral return current region, Ph.D. thesis, Boston Coll., Boston, Mass., 1986.
- Ganguli, S. B., and P. J. Palmadesso, Plasma transport in the auroral return current region, *J. Geophys. Res.*, **92**, 8673, 1987.
- Ganguli, S. B., H. G. Mitchell, and P. J. Palmadesso, Behavior of ionized plasma in the high latitude topside ionosphere: The polar wind, *Planet. Space Sci.*, **35**, 703, 1987.
- Gombosi, T. I., and T. L. Killeen, Effects of thermospheric motions on the polar wind: A time-dependent numerical study, *J. Geophys. Res.*, **92**, 4725, 1987.
- Gombosi, T. I., and R. W. Schunk, A comparative study of plasma expansion events in the polar wind, *Planet. Space Sci.*, **36**, 753, 1988.
- Gombosi, T. I., T. E. Cravens, and A. F. Nagy, A time-dependent theoretical model of the polar wind: Preliminary results, *Geophys. Res. Lett.*, **12**, 167, 1985.
- Ho, C. W., J. L. Horwitz, G. R. Wilson, N. Singh, and T. E. Moore, Effects of magnetospheric electrons on polar plasma outflow: A semikinetic model, *J. Geophys. Res.*, **97**, 8425, 1992.
- Ho, C. W., J. L. Horwitz, and G. R. Wilson, Dynamics of the H^+ and O^+ polar wind in the transition region as influenced by ionospheric convection and electron heating, *J. Geophys. Res.*, **102**, 395, 1997.
- Hoffman, J. H., Studies of the composition of the ionosphere with a magnetic deflection mass spectrometer, *Int. J. Mass Spectrom. Ion Phys.*, **4**, 315, 1970.
- Hoffman, J. H., and W. H. Dodson, Light ion concentrations and fluxes during magnetically quiet times, *J. Geophys. Res.*, **85**, 626, 1980.
- Hoffman, J. H., W. H. Dodson, C. R. Lippincott, and H. D. Hammack, Initial ion composition results from ISIS 2 satellite, *J. Geophys. Res.*, **79**, 4246, 1974.
- Holzer, T. E., J. A. Fedder, and P. M. Banks, A comparison of kinetic and hydrodynamic models of an expanding ion-exosphere, *J. Geophys. Res.*, **76**, 2453, 1971.
- Horwitz, J. L., C. J. Pollock, T. E. Moore, W. K. Peterson, J. L. Burch, J. D. Winningham, J. D. Craven, L. A. Frank, and A. Persoon, The polar cap environment of outflowing O^+ , *J. Geophys. Res.*, **97**, 8361, 1992.
- Khazanov, G. V., T. Neubert, G. D. Gefan, Kinetic theory of ionosphere-plasmasphere transport of suprathermal electrons, *IEEE Trans. Plasma Sci.*, **22**, 187, 1994.
- Lee, J. S., J. P. Doering, T. A. Potemra, and L. H. Brace, Measurements of the ambient photoelectron spectrum from Atmosphere Explorer II: AE-E measurements from 300 to 1000 km during solar minimum conditions, *Planet. Space Sci.*, **28**, 973, 1980.
- Lemaire, J., Effect of escaping photoelectrons in a polar exospheric model, *Space Res.*, **12**, 1413, 1972.
- Lemaire, J., and M. Scherer, Model of the polar ion-exosphere, *Planet. Space Sci.*, **18**, 103, 1970.
- Lemaire, J., and M. Scherer, Kinetic models of the solar and polar wind, *Rev. Geophys.*, **11**, 427, 1973.
- Li, P., G. R. Wilson, J. L. Horwitz, and T. E. Moore, Effect of mid-altitude ion heating on ion outflow at polar latitudes, *J. Geophys. Res.*, **93**, 9753, 1988.
- Loranc, M., W. B. Hanson, R. A. Heelis, and J.-P. St.-Maurice, A morphological study of vertical ionospheric flows in the high-latitude *F* region, *J. Geophys. Res.*, **96**, 3627, 1991.
- Marubashi, K., Escape of the polar-ionospheric plasma into the magnetospheric tail, *Rep. Ionos. Space Res. Jpn.*, **24**, 322, 1970.
- Moore, T. E., Modulation of terrestrial ion escape compo-

- sition (by low-altitude acceleration and charge exchange chemistry), *J. Geophys. Res.*, **85**, 2011, 1980.
- Moore, T. E., et al., High altitude observations of the polar wind, *Science*, **277**, 349, 1997.
- Nagai, T., J. H. Waite Jr., J. L. Green, C. R. Chappell, R. C. Olsen, and R. H. Comfort, First measurements of supersonic polar wind in the polar magnetosphere, *Geophys. Res. Lett.*, **11**, 669, 1984.
- Newell, P. T., D. G. Sibeck, and C.-I. Meng, Penetration of the interplanetary magnetic field B_y and magnetosheath plasma into the magnetosphere: Implications for the predominant magnetopause merging site, *J. Geophys. Res.*, **100**, 235, 1995.
- Olsen, R. C., C. R. Chappell, and J. L. Burch, Aperture plane potential control for thermal ion measurements, *J. Geophys. Res.*, **91**, 3117, 1986.
- Ottley, J. A., and R. W. Schunk, Density and temperature structure of helium ions in the topside polar ionosphere for subsonic outflows, *J. Geophys. Res.*, **85**, 4177, 1980.
- Pollock, C. J., C. R. Chappell, J. L. Horwitz, and J. D. Winningham, Two-spacecraft charged particle observations interpreted in terms of electrostatic potential drops along polar cap field lines, in *Modeling Magnetospheric Plasma Processes*, *Geophys. Monogr. Ser.*, vol. 62, edited by G. R. Wilson, p.111, AGU, Washington, D. C., 1991.
- Puri, S., Plasma heating and diffusion in stochastic fields, *Phys. Fluids*, **9**, 2043, 1966.
- Raitt, W. J., R. W. Schunk, and P. M. Banks, A comparison of the temperature and density structure in the high and low speed thermal proton flows, *Planet. Space Sci.*, **23**, 1103, 1975.
- Raitt, W. J., R. W. Schunk, and P. M. Banks, The influence of convection electric fields on thermal proton outflow from the ionosphere, *Planet. Space Sci.*, **23**, 291, 1977.
- Raitt, W. J., R. W. Schunk, and P. M. Banks, Quantitative calculations of helium ion escape fluxes from the polar ionosphere, *J. Geophys. Res.*, **83**, 5617, 1978a.
- Raitt, W. J., R. W. Schunk, and P. M. Banks, Helium ion outflow from the terrestrial ionosphere, *Planet. Space Sci.*, **26**, 255, 1978b.
- Richards, P. G., and D. G. Torr, Ratios of photoelectron to EUV ionization rates for aeronomic studies, *J. Geophys. Res.*, **93**, 4060, 1988.
- Richards, P. G., J. A. Fennelly, and D. G. Torr, EUVAC: A solar EUV flux model for aeronomic calculations, *J. Geophys. Res.*, **99**, 8981, 1994.
- Schunk, R. W., and A. F. Nagy, Electron temperatures in the F region of the ionosphere: Theory and observations, *Rev. Geophys.*, **16**, 355, 1978.
- Schunk, R. W., and J. J. Sojka, A three-dimensional time-dependent model of the polar wind, *J. Geophys. Res.*, **94**, 8973, 1989.
- Schunk, R. W., and D. S. Watkins, Electron temperature anisotropy in the polar wind, *J. Geophys. Res.*, **86**, 91, 1981.
- Schunk, R. W., and D. S. Watkins, Proton temperature anisotropy in the polar wind, *J. Geophys. Res.*, **87**, 171, 1982.
- Shodhan, S., G. L. Siscoe, L. A. Frank, K. L. Ackerson, W. R. Paterson, D. Fairfield, S. Kokubun, and T. Yamamoto, Mantle crossing at geotail: Comparison with MHD model, *J. Geophys. Res.*, **101**, 153, 1996.
- Sibeck, D. G., and J. T. Gosling, Magnetosheath density fluctuations and magnetopause motion, *J. Geophys. Res.*, **101**, 31, 1996.
- Singh, N., and R. W. Schunk, Temporal evolution of density perturbations in the polar wind, *J. Geophys. Res.*, **90**, 6487, 1985.
- Sturrock, P. A., Stochastic accelerations, *Phys. Rev.*, **141**, 186, 1966.
- Su, Y.-J., J. L. Horwitz, C. W. Ho, P. G. Richards, and G. R. Wilson, A coupled fluid-semikinetic treatment for ionospheric plasma outflow: First results (abstract), *Eos Trans. AGU*, **76**(46), Fall Meet. Suppl., 505, 1995.
- Su, Y.-J., J. L. Horwitz, M. Hirahara, T. E. Moore, M. O. Chandler, B. L. Giles, P. D. Craven, C. J. Pollock, and J. Scudder, Survey of the polar wind from 5000 km to 8 R_E altitude with POLAR TIDE/PSI (abstract), *Eos Trans. AGU*, **78**(17), Spring Meet. Suppl., S294, 1997.
- Tam, S. W. Y., F. Yasseen, T. Chang, and S. B. Ganguli, Self-consistent kinetic photoelectron effects on the polar wind, *Geophys. Res. Lett.*, **22**, 2107, 1995.
- Torr, M. R., D. G. Torr, P. G. Richards, and S. P. Yung, Mid- and low-latitude model of thermospheric emissions, 1, $O^+(^2P)$ 7320 Å and $N_2(^2P)$ 3371 Å, *J. Geophys. Res.*, **95**, 21,147, 1990.
- Wilson, G. R., Scmikinetic modeling of the outflow of ionospheric plasma through the topside collisional to collisionless transition region, *J. Geophys. Res.*, **97**, 10,551, 1992.
- Wilson, G. R., Kinetic modeling of O^+ outflow resulting from $E \times B$ convection heating in the high-latitude F region ionosphere, *J. Geophys. Res.*, **99**, 17,453, 1994.
- Wilson, G. R., Development of non-Maxwellian velocity distributions as a consequence of nonlocal Coulomb collision, in *Cross-Scale Coupling in Space Plasma*, *Geophys. Monogr. Ser.*, vol. 93, edited by J. L. Horwitz, N. Singh, and J. Burch, p.47, AGU, Washington, D. C., 1995.
- Wilson, G. R., C. W. Ho, J. L. Horwitz, N. Singh, and T. E. Moore, A new kinetic model for time-dependent polar plasma outflow: Initial results, *Geophys. Res. Lett.*, **17**, 263, 1990.
- Wilson, G. R., G. Khazanov, and J. L. Horwitz, Achieving zero current on open flux tubes carrying large photoelectron fluxes, *Geophys. Res. Lett.*, **24**, 1183, 1997.
- Winningham, J. D., and C. Gurgiolo, DE-2 photoelectron measurements consistent with a large scale parallel electric field over the polar cap, *Geophys. Res. Lett.*, **9**, 977, 1982.
- Winningham, J. D., and W. J. Heikkila, Polar cap auroral electron fluxes observed with ISIS 1, *J. Geophys. Res.*, **79**, 949, 1974.
- Yasseen, F., J. M. Rettcrer, T. Chang, and J. D. Winningham, Monte-Carlo modeling of polar wind photoelectron distributions with anomalous heat flux, *Geophys. Res. Lett.*, **16**, 1023, 1989.
- Yau, A. W., P. H. Beckwith, W. K. Peterson, and E. G. Shelley, Long-term (solar cycle) and seasonal variations of upflowing ionospheric ion events at DE 1 altitudes, *J. Geophys. Res.*, **90**, 6395, 1985.
- Yau, A. W., T. Abe, T. Chang, T. Mukai, K. I. Oyama, and B. A. Whalen, Akebono observations of electron temperature anisotropy in the polar wind, *J. Geophys. Res.*, **100**, 17,451, 1995.

D. G. Brown, J. L. Horwitz, P. G. Richards, Y.-J. Su, Center for Space Plasma and Aeronomic Research, The University of Alabama in Huntsville, Huntsville, AL 35899. (e-mail: brownnd@cspar.uah.edu; horwitzj@cspar.uah.edu; richardsp@cspar.uah.edu; suy@cspar.uah.edu)

C. W. Ho, Department of Physics, Prairie View A&M University, Prairie View, Texas 77446. (e-mail: wing@spc.prsci.pramu.edu)

G. R. Wilson, Mission Research Corporation, One Tara Blvd., Suite 302, Nashua, NH 03062. (e-mail: gwilson@mrcnh.com)

(Received April 4, 1997; revised October 21, 1997; accepted October 23, 1997.)